

Ab-initio no-core shell model study of $^{18-24}\text{Ne}$ isotopes

Chandan Sarma^{1,*} and Praveen C. Srivastava^{1,†}

¹*Department of Physics, Indian Institute of Technology Roorkee, Roorkee 247667, India*

(Dated: August 2, 2022)

We report *ab initio* no-core shell model (NCSM) study of $^{18-24}\text{Ne}$ isotopes for energy spectra, electromagnetic properties, and point-proton radii using four realistic NN interactions. We have used inside nonlocal outside Yukawa (INOY), charge-dependent Bonn 2000 (CDB2K), the chiral next-to-next-to-next-to-leading order ($N^3\text{LO}$) and optimized next-to-next-to-leading order ($N^2\text{LO}_{opt}$) interactions. We are able to reach basis size up to $N_{max} = 6$ for ^{18}Ne and $N_{max} = 4$ for the $^{19-24}\text{Ne}$ isotopes with m-scheme dimensions up to 1.0×10^9 in case of ^{24}Ne . We observed better results for INOY interaction in terms of the binding energies of ground state (g.s.), and overall all the four interactions provide good agreement with the experimental low-energy spectra. Our results for reduced $M1$ transition strengths and magnetic moments are close to the experimental values. We found that for long-range observables such as the $E2$ transition strengths, the electric quadrupole moments, and the point-proton radii (r_p), we need higher N_{max} calculations to obtain results comparable to the experimental data. We have observed almost 6 % increment in the converged r_p as we increase the model space from $N_{max} = 4$ to $N_{max} = 6$.

I. INTRODUCTION

Atomic nuclei are quantum many-body systems, and understanding nuclear properties from first principles is one of the main goal of low-energy nuclear physics. This motivation is fulfilled by the *ab initio* approaches [1–4], which aim to describe different nuclear phenomena based on the fundamental interactions among the nucleons [5, 6]. The growth in computing power in recent times has opened the path to apply different *ab initio* approaches to investigate nuclear structure properties [7]. These approaches involve sophisticated methods to solve the non-relativistic many-particle Schrödinger equation by taking nucleon-nucleon interaction as the input. The modern nuclear interactions are either derived from the meson exchange theory [8] or Quantum Chromodynamics (QCD) [9] based on chiral effective field theory (χEFT) [10–13]. Due to the complex nature of nuclear interaction, the application of *ab initio* approaches to nuclear physics is a challenging task.

Being one of the *ab initio* approaches, the no-core shell model (NCSM) [1, 14] is a fundamental approach in comparison to the conventional nuclear shell model [15–20]. The NCSM is able to explain different properties of nuclei in the lighter-mass region [21–28]. In this paper our aim is to study $^{18-24}\text{Ne}$ isotopes from the neutron shell closure at $N = 8$ to $N = 14$ for different nuclear properties. The neon isotopic chain exhibit novel structures, starting from the Borromean structure of ^{17}Ne [29] which is considered to be a candidate for two-proton halo structure, clustering in the ground-state of ^{20}Ne doubly open-shell isotope to the neutron-rich ^{30}Ne around which the island of inversion occurs. In the past, the study on $^{20-22}\text{Ne}$ isotopes was carried out for level structures, and electromagnetic transitions within the shell-model approach

[30, 31]. In Ref. [32], the isospin dependence of deformation is studied for carbon and neon isotopes. In this paper, the electromagnetic moments and transition strengths are calculated using the deformed Hartree-Fock (HF) model and compared with the standard shell model results. The significant contribution of the $^{16}\text{O} + \alpha$ cluster structure to the g.s. (0^+) of ^{20}Ne is discussed extensively in Refs. [33, 34]. The antisymmetrized molecular dynamics (AMD) method is used in Ref. [34] to study cluster structure of ^{20}Ne along with ^{12}C and ^{16}O nuclei. In Ref. [35], two *ab initio* methods, namely the quasi-exact in-medium no-core shell model (IM-NCSM) and the projected generator coordinate method (PGCM), are used to study even neon isotopes from ^{18}Ne to ^{32}Ne . Dytrych *et al.* use symmetry-adapted no-core shell model (SA-NCSM) in Ref. [36] to study the shape of ^{20}Ne g.s. and other excited states. The authors have used $\text{Sp}(3, \mathbb{R})$ -adapted basis for this work which reduces the size of the Hamiltonian matrix significantly, and a single symplectic basis provides information about nuclear dynamics. Recently, a machine learning (ML) technique based on neural network was developed using *ab initio* SA-NCSM results of some selected light nuclei as training data [37]. In the Ref. [38], *ab initio* no-core Monte Carlo shell model approach is used to calculate the ground-state energies and point-proton root-mean-square radii of light $4N$ self-conjugate nuclei up to ^{20}Ne . For this work, the authors employed two nonlocal NN interactions, namely JISP16 and Daejeon16. Stroberg, *et al.* [39] use the valence-space in-medium similarity renormalization group (VS-IMSRG) to evaluate the isospin dependence of the underprediction of $E2$ strength. For this purpose, different *sd*-shell nuclei, including $^{18,19,21,22}\text{Ne}$ isotopes, are used and they find out that the missing strength is mostly isoscalar in nature. Another approach, namely the energy density functional (EDF) framework, is used to study the even-neon isotopes starting from ^{20}Ne towards the dripline nucleus in Ref. [40]. The authors have investigated the evolution of cluster structure

* c.sarma@ph.iitr.ac.in

† Corresponding author: praveen.srivastava@ph.iitr.ac.in

in the even-even neon isotopes towards neutron drip line [41]. The experimental prediction of the neutron drip line for neon and fluorine has been performed recently at the RIKEN Radioactive Isotope Beam Factory by fragmentation of an intense beam of ^{48}Ca on a thick Be target [42]. This work indicates that ^{34}Ne is the heaviest bound isotope of the neon isotopic chain.

The charge radius of an atomic nucleus is another fundamental property that is helpful in understanding the nuclear structure. Due to the complex nature of nuclear interaction, the charge radius reflects several nuclear structure phenomena such as halo structures, the occurrence of magic numbers, shape staggering, shape coexistence, pairing correlations etc. [43]. Therefore, experimental measurements of charge radii along with theoretical validations and predictions are essential to understand nuclear structure properties. Different experimental methods are available to measure the charge radii of nuclei across the nuclear chart. Some methods like the e^- scattering experiments provide information about the charge radii directly. In contrast, other methods like the optical isotope shifts give information about isotopic changes of charge radii with respect to a stable isotope. These two types of experiments are complementary, and they can provide valuable information for charge radii of nuclei [44]. In Ref. [45], high-precision mass and charge radius of $^{17-22}\text{Ne}$ are measured using Penning trap mass spectroscopy and collinear laser spectroscopy. This paper mainly discusses the charge radius of two-proton-halo candidate ^{17}Ne , which shows an unusually large charge radius than the other members of that isotopic chain. K. Marinova, *et. al.* in Ref. [46], measured the changes in mean-square charge radii of neon isotopes from ^{17}Ne up to ^{28}Ne with respect to the stable ^{20}Ne isotope using laser spectroscopy measurements. In Ref. [47], charge radii of neon and magnesium isotopes are calculated along with the ground-state energies and two neutron separation energies using *ab initio* coupled-cluster (CC) theory. In this work, the authors have used NN and $3N$ potentials mainly based on $\Delta\text{NNLO}_{\text{CO}}$ interaction. Like the charge radii, determining point proton radii of neutron-rich nuclei provides valuable information about the underlying structure. The point proton radii of $^{17-22}\text{N}$ were measured experimentally for the first time in Ref. [48] by measuring the charge changing cross-sections (σ_{cc}). The r_p measured from σ_{cc} are compared with the direct measurement of r_p from e^- scattering and theoretical predictions from the shell model and *ab initio* approaches: VS-IMSRG and coupled-cluster (CC) method. All this information shows a local minimum of r_p at ^{21}N and the evolution of a halo-like structure of ^{22}N . These two observations hint at a shell gap at $N = 14$ in the nitrogen isotopic chain.

In this work, our aim is to study $^{18-24}\text{Ne}$ isotopes within the framework of NCSM using INOY [49], CDB2K [50], chiral N^3LO [51] and $\text{N}^2\text{LO}_{\text{opt}}$ [52] NN interactions. For ^{18}Ne , we have reached basis size up to $N_{\text{max}} = 6$ and for the rest of the neon isotopes basis size up to N_{max}

$= 4$ have been reached. We have reached the highest scheme dimension 1.0×10^9 for $N_{\text{max}} = 4$ in the case of ^{24}Ne . In addition to the low-lying energy spectra of these neon isotopes, we have also calculated electromagnetic properties and point-proton radii.

This paper is organized as follows: In Sec. II, we briefly describe the basic formalism of the NCSM approach. Different NN interactions used in this paper are described briefly in Sec. III. In Sec. IV, the NCSM results for energy spectra are presented. The NCSM results of the electromagnetic properties and the point-proton radii are discussed in Sec. V and Sec. VI, respectively. Finally, we have summarized our work in Sec. VII.

II. NO-CORE SHELL MODEL FORMALISM

The no-core-shell model (NCSM) [1, 14] is an *ab initio* approach which is very successful in describing nuclear properties in the lighter mass region. It is a non-perturbative approach in which a system of non-relativistic nucleons are considered that interact via realistic NN or $NN+3N$ interactions among themselves. Unlike the conventional shell model, there is no core in this approach, and all the nucleons are considered active.

The NCSM Hamiltonian considering only realistic NN interactions among the nucleons, is given by

$$H_A = T_{\text{rel}} + V = \frac{1}{A} \sum_{i < j}^A \frac{(\vec{p}_i - \vec{p}_j)^2}{2m} + \sum_{i < j}^A V_{ij}^{NN} \quad (1)$$

where, T_{rel} denotes the relative kinetic energy, $p_{i,j}$ ($i, j = 1, 2, 3, \dots, A$) is momentum of a single nucleon, m is the mass of nucleon and V_{ij}^{NN} is the NN interaction which contains the nuclear part along with the Coulomb part.

In the NCSM, the eigenstates of the Hamiltonian are determined by solving a large-scale matrix eigenvalue problem within a model space spanned by a set of many-body states. The model space of the NCSM is constructed by taking Slater determinants of the harmonic-oscillator single-particle states having N_{max} -truncation on the many-body states. The truncation parameter N_{max} measures the allowed harmonic-oscillator quanta above the unperturbed g.s. of an A-nucleon system. The use of harmonic-oscillator basis along with $N_{\text{max}}\hbar\Omega$ truncation allows the separation of the intrinsic component of the many-body basis from the center-of-mass component for all N_{max} . In order to treat the original Hamiltonian (1) in a truncated HO basis, it is necessary to derive the effective interaction suitable for the basis truncation. Some renormalization techniques based on similarity transformation are necessary to obtain an effective interaction. Two such techniques that are utilized in the NCSM are: the Okubo-Lee-Suzuki (OLS) [53–56] scheme and the similarity renormalization group (SRG) [57, 58].

We have used the OLS scheme to derive effective interactions in this work. The derivation of the effective interaction involves the modification of the original Hamilto-

nian (1) by adding to it the center-of-mass Hamiltonian (H_{cm}):

$$H_A^\Omega = H_A + H_{CM} = \sum_{i=1}^A \left[\frac{p_i^2}{2m} + \frac{1}{2} m \Omega^2 r_i^2 \right] + \sum_{i < j}^A \left[V_{NN,ij} - \frac{m \Omega^2}{2A} (r_i - r_j)^2 \right] \quad (2)$$

where, $H_{CM} = T_{CM} + U_{CM}$. As H_A is a translational invariant Hamiltonian, the addition of H_{CM} to it does not change the fundamental property of the system, and it is subtracted out in a subsequent step. The effective Hamiltonian contains all the terms up to A-body, even if the original Hamiltonian consist of only two-body terms. As we have considered only the two-body part of the Hamiltonian, we expect that the two-body part of the effective interaction will be the dominant part of the exact effective interaction. So, in this work, only the two-body OLS effective interactions are taken into account, and it is obtained by solving the Hamiltonian (2) exactly for a two nucleon system.

In the final step, the c.m. Hamiltonian $H_{c.m}$ is subtracted out from Hamiltonian (2) and the Lawson projection term [59] $\beta(H_{c.m} - \frac{3}{2}\hbar\Omega)$ is added to it. In this work, the value of β is taken to be 10. As the effective interaction is translationally invariant, the addition of the Lawson projection term does not shift the physical energy states having a passive state of the c.m. motion. However, it does shift the states with excited c.m. motion to a higher value, so that there is no mixing of the physically relevant states and the states with excited c.m. motion. In the OLS scheme, the infinite A-nucleon HO basis is divided into the finite active space (P) consisting of all states up to N_{max} HO excitations and the excluded space ($Q = 1 - P$). The effective Hamiltonian for the A-nucleon system, considering only the two-body effective interaction, is given by:

$$H_{A,\text{eff}}^\Omega = P \left\{ \sum_{i < j}^A \left[\frac{(\vec{p}_i - \vec{p}_j)^2}{2mA} + \frac{m\Omega^2}{2A} (\vec{r}_i - \vec{r}_j)^2 \right] + \sum_{i < j}^A \left[V_{ij}^{NN} - \frac{m\Omega^2}{2A} (\vec{r}_i - \vec{r}_j)^2 \right]_{\text{eff}} + \beta \left(H_{c.m.} - \frac{3}{2}\hbar\Omega \right) \right\} P. \quad (3)$$

The effective interaction of Eq. (3) depends on nucleon number A, the HO frequency Ω and the basis size of the P-space controlled by N_{max} . In order to minimize the effect of neglected higher clusters in the derivation of effective Hamiltonian, large model space is needed. For the case of $N_{max} \rightarrow \infty$, the NCSM effective Hamiltonian given above approaches the bare Hamiltonian (1). Accordingly, the NCSM results converge to the exact solution as the basis size increases [24].

III. NN INTERACTIONS

In our present work, we have used four realistic NN interactions namely, inside nonlocal outside Yukawa (INOY) [49, 60, 61], charge dependent Bonn NN interaction (CDB2K) [8, 50, 62, 63], N³LO [9, 51] and N²LO_{opt} [52, 64].

The inside nonlocal outside Yukawa (INOY) [49, 60, 61] is a phenomenological potential with a nonlocal part at a short distance (≤ 1 fm). At a large distance (≥ 3 fm), it becomes the Yukawa tail of local Argonne v18 [65] potential. The nonlocality of nuclear interactions at short distances is primarily due to the internal structure of the nucleon. There is a smooth cutoff in the transition region (1-3 fm) from the local to the nonlocal part, and the range of locality and nonlocality can be controlled explicitly. This NN interaction is defined as

$$V_{ll'}^{full}(r, r') = W_{ll'}(r, r') + \delta(r - r') F_{ll'}^{cut}(r) V_{ll'}^{Yukawa}(r)$$

where, the cut-off function is

$$F_{ll'}^{cut}(r) = \begin{cases} 1 - e^{-[\alpha_{ll'}(r - R_{ll'})]^2} & \text{for } r \geq R_{ll'}, \\ 0 & \text{for } r \leq R_{ll'}, \end{cases}$$

and $W_{ll'}(r, r')$ and $V_{ll'}^{Yukawa}(r)$ are the phenomenological nonlocal part and the local Yukawa tail of Argonne v18 potential, respectively. The parameters $\alpha_{ll'}$ and $R_{ll'}$ are considered to be independent of the angular momenta having values 1.0 fm⁻¹ and 1.0 fm, respectively. The other parameters of $W_{ll'}(r, r')$ are determined by fitting NN data and the binding energy of ³He. This interaction model breaks charge independence and charge symmetry as it is essential to reproduce all low-energy experimental parameters, including *np*, *pp*, and *nn* scattering lengths to high precision. To describe a few-nucleon system reasonably well, additional 3N forces are necessary along with local NN potentials, but INOY NN interaction does not need 3N force to provide the binding energies of 3N systems. The effects of three-nucleon forces are partly included in the non-local part of this interaction.

The charge-dependent Bonn 2000 (CDB2K)[50, 62, 63] is a one-boson exchange NN potential which includes all the mesons π , η , ρ , and ω with masses below the nucleon mass. Due to the vanishing coupling of η -meson to the nucleon, it is dropped from the potential model. In addition to these mesons, two partial-wave dependent scalar-isoscalar σ bosons are also introduced. This charge-dependent potential reproduces accurately charge symmetry breaking (CSB) and charge independence breaking (CIB) in all partial waves with $J \leq 4$ as predicted by the Bonn full model [8]. In this model, three NN interactions are constructed: a proton-proton, a neutron-neutron, and a neutron-proton potential, and the differences between them are measured by CSB and CIB.

These potentials fit the world proton-proton data available in the year 2000 with $\chi^2/\text{datum} = 1.01$ and the corresponding neutron-proton data with $\chi^2/\text{datum} = 1.02$ below 350 MeV. The CDB2K potential uses the original form of the covariant Feynman amplitudes of meson exchange without local approximation. So, the off-shell behavior of this NN potential is different from other local NN potentials.

The chiral NN interaction at next-to-next-to-next-to-leading order ($N^3\text{LO}$) [51] is derived from the quantum chromodynamics using chiral perturbation theory (χPT). The χPT is a systematic expansion of the nuclear potential in terms of $(Q/\Lambda_\chi)^\nu$, where Q is a low-momentum scale or pion mass, $\Lambda_\chi \approx 1$ GeV is the chiral symmetry breaking scale and $\nu \geq 0$ [9]. For a definite order ν , there is a finite number of unique and calculable contributing terms. The long-ranged part of the nuclear interaction is associated with the exchange of pions, whereas the short-ranged part is defined in terms of contact terms. The charge dependence of this interaction is important for a good fit of the low-energy pp and np data. There are, in total, 29 parameters of the $N^3\text{LO}$ potential. Three of them are low-energy constants (LECs), c_2 , c_3 and c_4 that appear in the πN Lagrangians. The most important fit parameters are 24 contact terms that dominate the partial waves with $L \leq 2$, and the remaining two parameters are two charge-dependent contact terms. The NN interaction at this order can be compared to high-precision phenomenological potential AV18 [65] in terms of the accuracy in reproducing the NN data below 290 MeV lab-energy.

The $N^2\text{LO}_{opt}$ [52, 64] is a chiral NN interaction optimized at next-to-next-to-leading order ($N^2\text{LO}$) using the optimizing tool POUNDERS. Using this derivative-free algorithm, the three πN low-energy constants (c_1 , c_3 , c_4) along with 11 contact parameters C and \tilde{C} related to partial waves are optimized. The $N^2\text{LO}_{opt}$ NN interaction yields $\chi^2/\text{datum} \approx 1$ for laboratory energies below 125 MeV. This interaction reproduces the experimental binding energies and radii of $A = 3, 4$ systems. The $N^2\text{LO}_{opt}$ is a soft potential, and renormalization techniques like SRG or OLS are not necessary in order to obtain converged results.

The NCSM results reported in this paper have been calculated using the pAntoine [66–68] code. Our group has previously reported the NCSM results for N [69], O [70], F [70] and B [71] isotopes.

TABLE I. The m-scheme dimensions of Ne isotopes corresponding to different N_{max} are shown. The dimensions up to which we have reached are shown in blue.

N_{max}	^{18}Ne	^{19}Ne	^{20}Ne	^{21}Ne	^{22}Ne	^{23}Ne	^{24}Ne
0	14	128	640	1935	4206	6457	7562
2	2.7×10^4	1.4×10^5	5.4×10^5	1.5×10^6	3.1×10^6	5.0×10^6	6.5×10^6
4	5.1×10^6	2.2×10^7	7.5×10^7	1.9×10^8	4.1×10^8	7.1×10^8	1.0×10^9
6	3.4×10^8	1.3×10^9	4.4×10^9	1.1×10^{10}	2.5×10^{10}	4.5×10^{10}	6.8×10^{10}
8	1.2×10^{10}	4.7×10^{10}	1.5×10^{11}	4.0×10^{11}	9.0×10^{11}	1.7×10^{12}	2.7×10^{12}

IV. RESULTS AND DISCUSSIONS

In this section, we have presented the NCSM results of neon isotopes. The m-scheme dimensions for $^{18-24}\text{Ne}$ isotopes corresponding to different N_{max} are shown in Table I. The table shows that dimension of Hamiltonian matrix of Ne isotopes increases rapidly with the increase in N_{max} and the number of nucleons, A . We are able to reach basis size up to $N_{max} = 6$ for ^{18}Ne and $N_{max} = 4$ for the remaining neon isotopes. The first step in the NCSM calculations is to obtain the optimum frequency for the g.s. energy, i.e., that frequency for which the g.s. energy is minimum for the maximum possible N_{max} . To obtain the optimum frequency for a particular interaction, the calculated g.s. energies for a particular nucleus are plotted with HO frequencies for different N_{max} . Fig. 1 shows the variation of g.s. energies of ^{18}Ne and ^{19}Ne with frequency for different N_{max} . For ^{18}Ne , we show the variation from $N_{max} = 0$ to 6; while for ^{19}Ne the variation from $N_{max} = 0$ to 4 are shown. Similarly, the variation of ground-state energies with HO frequency for other neon isotopes can be obtained. One general feature for all the four interactions we have considered is that the g.s. energy dependence on frequency becomes minimum for the largest possible N_{max} for all these isotopes. From Fig. 1, we obtain the optimal frequencies for INOY, CDB2K, $N^3\text{LO}$ and $N^2\text{LO}_{opt}$ for ^{18}Ne as 20, 14, 12 and 20 MeV, respectively. Similarly, it is possible to find the optimal frequencies for other neon isotopes corresponding to different NN interactions. In Fig. 1, the g.s. energies obtained from $N^2\text{LO}_{opt}$ interaction is variational with HO frequency, $\hbar\Omega$ and basis truncation parameter, N_{max} . The $N^2\text{LO}_{opt}$ interaction being a soft potential, OLS renormalization technique is not used. The g.s. energies obtained from other three OLS renormalized interactions are non-variational with $\hbar\Omega$ and N_{max} [1].

In Figs. 2-4, we have shown the low-lying spectra of different neon isotopes. For INOY interaction, we have shown spectra from 0 to the highest N_{max} , and for other realistic interactions, we have shown only the results for the highest N_{max} . Those results are compared with experimental data available for those nuclei.

A. Energy spectra of $^{18,20,22,24}\text{Ne}$

For ^{18}Ne , the ordering of the three lowest-lying states $0_1^+ - 2_1^+ - 4_1^+$, is well reproduced by NCSM calculations using INOY and $N^2\text{LO}_{opt}$ interactions as it can be seen from the first panel of Fig. 2. However, the separation between the g.s. and the 2_1^+ obtained from these two interactions are small compared to the experimental value (1.887 MeV). The other two interactions, CDB2K and $N^3\text{LO}$ can reproduce only the g.s. and the first excited state correctly. The excitation energy of the 2_1^+ obtained using $N^3\text{LO}$ (1.887 MeV) matches the experimental value. The energy separation between 4_1^+ and 2_1^+ obtained from INOY interaction decreases with basis

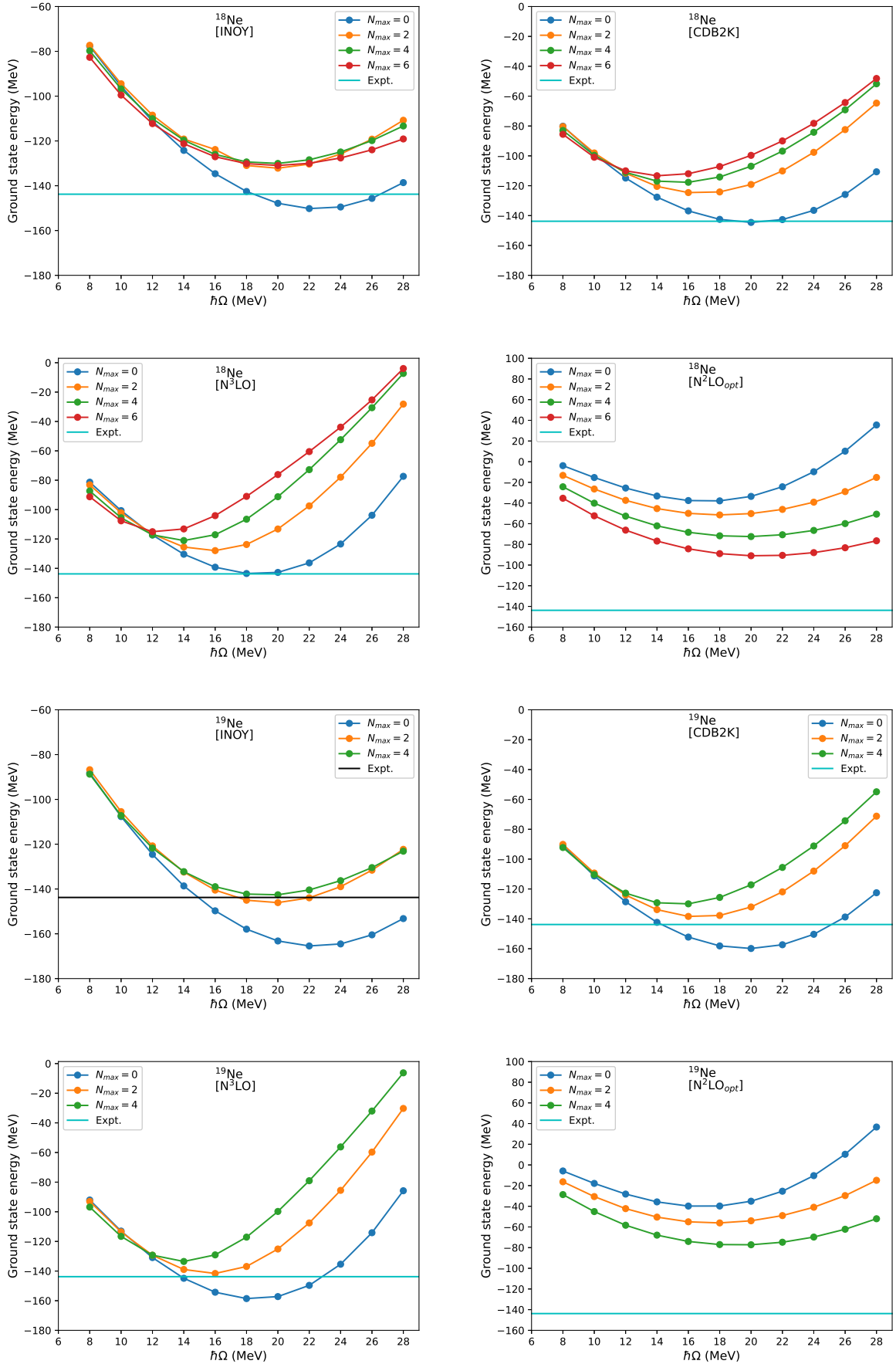
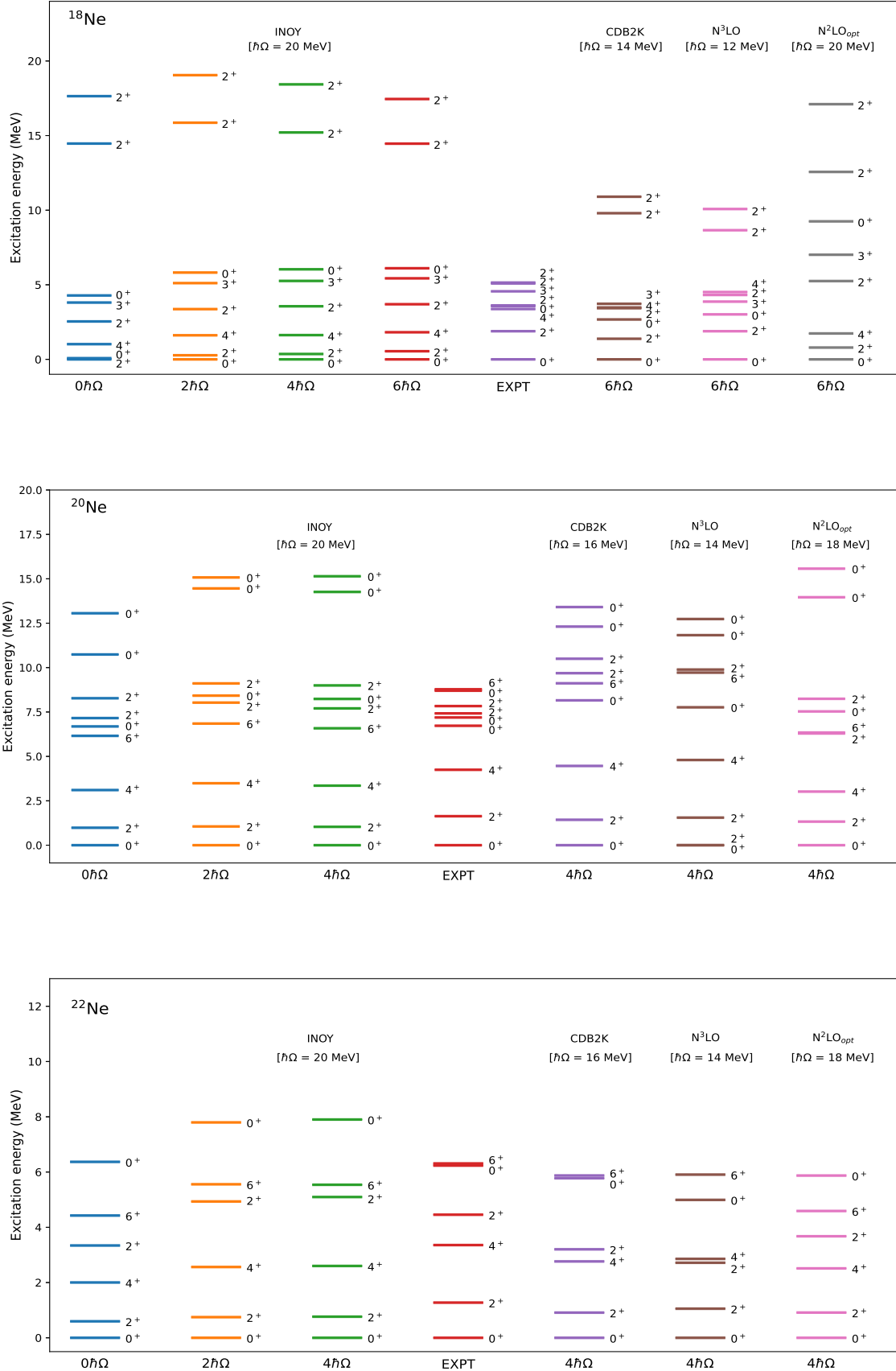


FIG. 1. Variation of the g.s. energies of ^{18}Ne and ^{19}Ne with HO frequency for different N_{max} .

FIG. 2. Low-lying energy spectra of $^{18,20,22}\text{Ne}$.

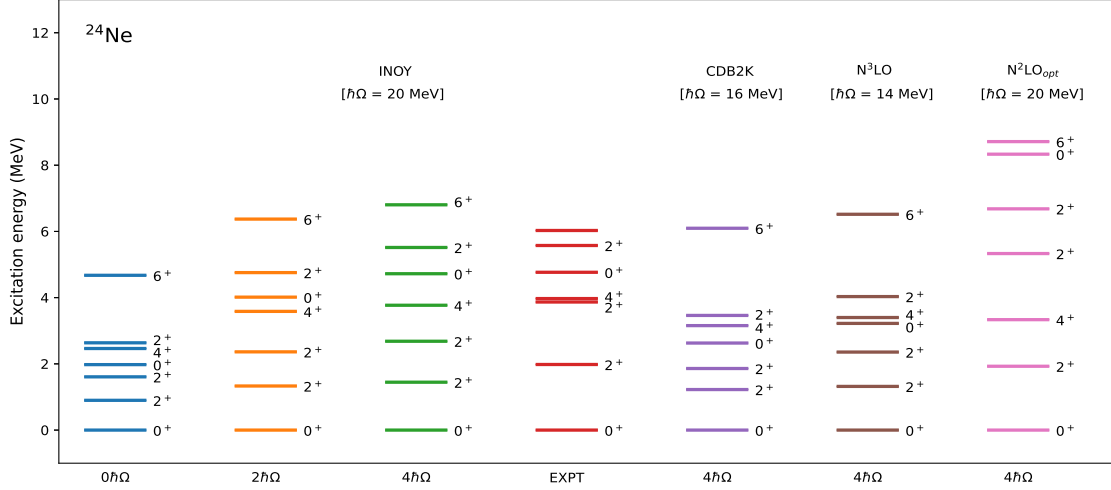


FIG. 3. Low-lying energy spectra of ^{24}Ne .

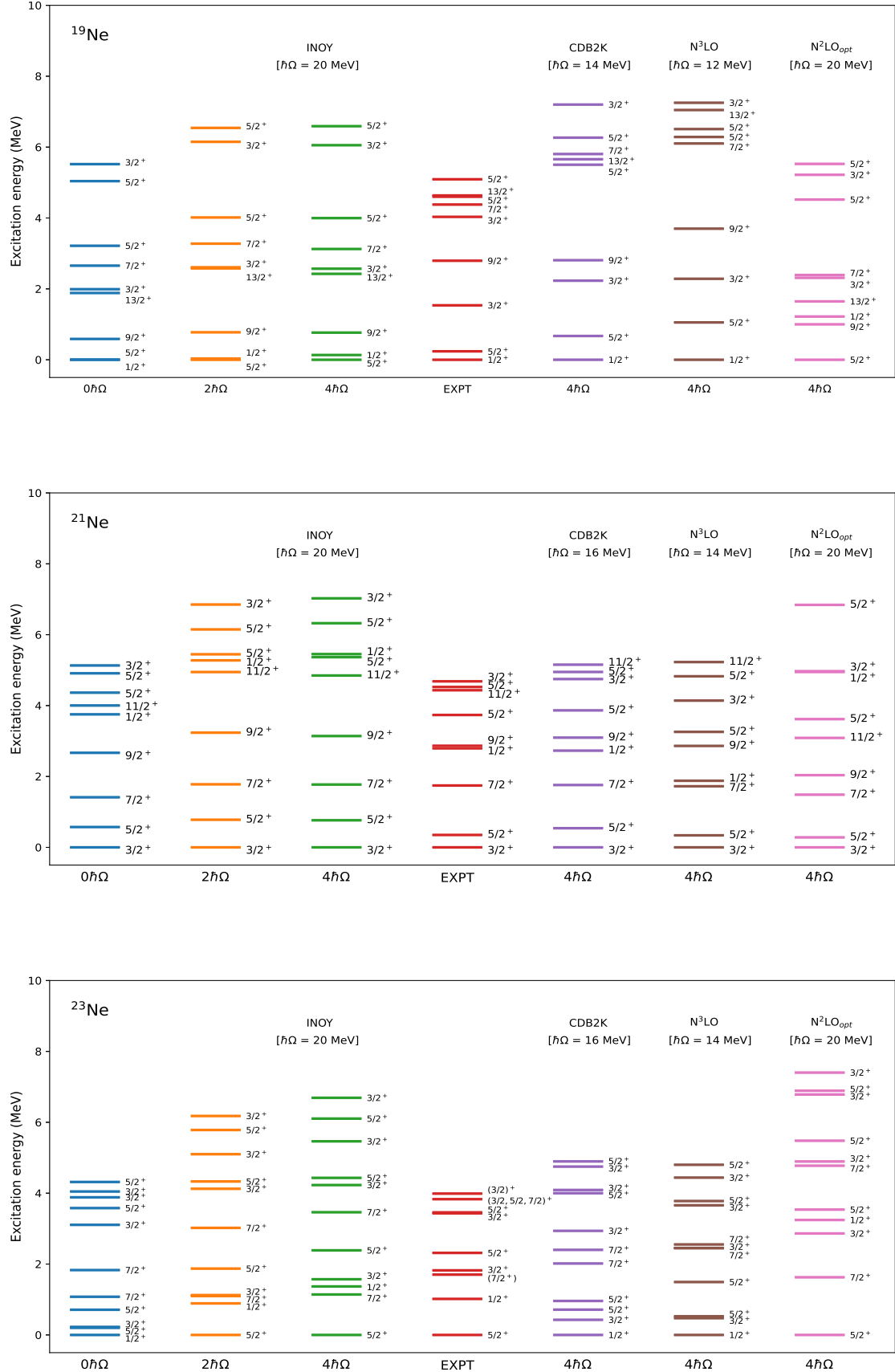
size increment and goes close to the experimental separation (1.489 MeV). Also, the 2_2^+ state obtained from the INOY is near the experimental one. The calculated energy separation between 4_1^+ and 2_2^+ states for N^3LO is close to the experimental separation though the ordering of these two states is reversed. The 4_1^+ state obtained for CDB2K is close to the experimental 4_1^+ state. Both 2_3^+ and 2_4^+ states obtained from all the four interactions are shifted upward compared to the experimental data. The 3_1^+ state calculated from INOY and $\text{N}^2\text{LO}_{opt}$ interactions are higher than the experimental value, whereas those calculated using CDB2K and N^3LO are lower than the experimental 3_1^+ state.

For ^{20}Ne , the excitation energy of the first excited state, 2^+ is 1.633 MeV. The calculated excitation energies of this state are obtained to be 1.034, 1.431, and 1.328 MeV from INOY, CDB2K, and $\text{N}^2\text{LO}_{opt}$ NN interactions, respectively. However, it is found to be very small (< 0.001 MeV) for N^3LO interaction. The correct ordering of $0_1^+-2_1^+-4_1^+-0_2^+$ states are obtained from CDB2K interaction, but the 0_2^+ state is shifted upward significantly compared to the experimental 0_2^+ state. The INOY and N^3LO interactions correctly reproduce spectra up to the second excited state, 4_1^+ . The 4_1^+ and 6_1^+ states obtained from CDB2K are near the experimental excitation energies. The separation between 0_3^+ and 0_4^+ states obtained for INOY, CDB2K, and N^3LO are almost the same, but it is smaller than the experimental value of separation (1.509 MeV) between those two states. From the second panel of Fig. 2, it can be seen that up to 5 MeV, the results of CDB2K are in good agreement with the experiment for ^{20}Ne .

Experimentally, the excitation energy of the first excited state, 2^+ of ^{22}Ne , is 1.274 MeV. The calculated

energy for this state is seen to be increasing slowly for INOY interaction with the increase in the basis size from $N_{max} = 0$ to $N_{max} = 4$ and approaching the experimental data. Similarly, the 4^+ state is also slowly shifted upwards towards the experimental excitation energy level with increasing basis size. All the interactions except N^3LO reproduce the correct ordering of states: $0_1^+-2_1^+-4_1^+-2_2^+$. The energy separation between the states 4_1^+ and 2_1^+ calculated by using INOY, CDB2K, and N^3LO are almost the same, which is slightly less than the experimental energy separation. The calculated energy separation between 6_1^+ and 0_2^+ for CDB2K is near the experimental energy difference between these two states. The separation between 6_1^+ and 2_2^+ from all the interactions except CDB2K is smaller than the experimental separation, and for CDB2K, it is larger than the experimental separation.

In the case of ^{24}Ne , the excited 2_1^+ , 2_2^+ , 4_1^+ , 0_2^+ , 2_3^+ states obtained from INOY interaction improve significantly with increasing the basis size from $N_{max}=0$ to 4 and approach the experimental data. More specifically, the 4_1^+ and 2_3^+ states from INOY go close to the experimental data. It can be seen from Fig. 3 that the INOY interaction reproduces the correct ordering of states: $0_1^+-2_1^+-2_2^+-4_1^+-0_2^+-2_3^+$, while CDB2K and N^3LO can reproduce correct ordering up to the second excited state, 2_2^+ . Similarly, $\text{N}^2\text{LO}_{opt}$ interaction can reproduce only the g.s. and the first excited state in correct ordering. The excitation energy of the first excited state, 2_1^+ obtained for $\text{N}^2\text{LO}_{opt}$ is close to the experimental excitation energy (1.981 MeV).

FIG. 4. Low-lying energy spectra of $^{19,21,23}\text{Ne}$.

B. Energy spectra of $^{19,21,23}\text{Ne}$

For ^{19}Ne , $1/2^+$ is the experimental g.s., and the excitation energy of the first excited state, $5/2^+$ is 0.238 MeV. The CDB2K and N^3LO interactions reproduce the correct g.s. and first excited state. The excitation energies of this first excited state obtained from these two interactions are 0.671 MeV and 1.053 MeV, respectively, which are greater than the experimental value. As shown in the second panel of Fig. 3, the CDB2K and N^3LO reproduce the correct ordering of states: $1/2_1^+ - 5/2_1^+ - 3/2_1^+ - 9/2_1^+$ and the energy separation between $3/2_1^+$ and $5/2_1^+$ for N^3LO is comparable to the experimental energy separation (1.298 MeV). However, the INOY and $\text{N}^2\text{LO}_{opt}$ interactions fail to predict the correct g.s. of ^{19}Ne . From the figure, it can be seen that the $9/2_1^+$ state obtained for CDB2K and the $5/2_2^+$ for $\text{N}^2\text{LO}_{opt}$ are close to the experimental data. The excitation energies of the high spin state $13/2_1^+$ obtained from INOY and $\text{N}^2\text{LO}_{opt}$ interactions are less than the experimental excitation energy. In contrast, for CDB2K and N^3LO , the excitation energy of this state is greater than the experimental data.

In the case of ^{21}Ne , the ordering of the low-lying energy states $3/2_1^+ - 5/2_1^+ - 7/2_1^+ - 1/2_1^+ - 9/2_1^+ - 5/2_1^+$ obtained from CDB2K and N^3LO interactions match with the experimental spectra. However, for INOY and $\text{N}^2\text{LO}_{opt}$ interactions, the ordering is correct only up to the second excited state. Experimentally, the excitation energy of the first excited state is 0.350 MeV, close to the energy (0.339 MeV) obtained from N^3LO interaction. The excitation energies of this state for other interactions are: 0.764, 0.540, and 0.282 MeV for INOY, CDB2K, and $\text{N}^2\text{LO}_{opt}$, respectively. For INOY interaction, the $7/2_1^+$ state goes up as we increase the basis size from $N_{max} = 0$ to 4 and is close to the experimental $7/2_1^+$ state. The calculated energies of the $7/2_1^+$ state from CDB2K and N^3LO interactions are also close to the experimental data. Similarly, the excitation energy of the $9/2_1^+$ state obtained from N^3LO is near the experimental energy data.

For ^{23}Ne , $5/2^+$ is the experimental g.s., and the INOY and $\text{N}^2\text{LO}_{opt}$ NN interactions correctly reproduce the g.s. The other two interactions fail to reproduce the correct g.s. for this nucleus. None of these four realistic interactions can predict the correct ordering of low-energy spectra. However, the $5/2_2^+$ state obtained for INOY and the $7/2_1^+$ for $\text{N}^2\text{LO}_{opt}$ are close to the corresponding experimental states. Experimentally, the $7/2_1^+$ is tentative, and our calculation with $\text{N}^2\text{LO}_{opt}$ confirms this state. The $3/2_1^+$ state for INOY shows a significant improvement with increasing basis size. Our result for this state is expected to be much closer to the experimental data once we increase the basis size. The $1/2_1^+$ state for $\text{N}^2\text{LO}_{opt}$ is pushed upward significantly compared to the experimental $1/2_1^+$ state.

V. ELECTROMAGNETIC PROPERTIES

In this section, the NCSM results for the g.s. energies and electromagnetic properties are discussed. In Table II, we summarise the calculated results of the g.s. energies ($E_{g.s.}$), reduced electric quadrupole transition probabilities $B(E2)$ and magnetic dipole transition probabilities $B(M1)$, quadrupole (Q) and magnetic moments (μ) for neon isotopes. The electromagnetic properties of the first excited states are shown in the table for even neon isotopes along with ^{19}Ne . For $^{21,23}\text{Ne}$, g.s. electromagnetic properties are shown. Available experimental results from Refs. [72, 73] are also included in this table for comparison. In this work, only one-body electromagnetic operators have been considered.

Experimentally, the g.s. binding energy of ^{18}Ne is -132.142 MeV, and the INOY interaction underbinds the g.s. by 1.187 MeV. The other realistic interactions underestimate the binding energy of ^{18}Ne more significantly. Similarly, the calculated g.s. energy of ^{19}Ne obtained from INOY interaction underbinds the g.s. by 1.061 MeV. Fig. 5 shows the mass number dependence of the calculated g.s. energies for neon isotopes along with the experimental results. The NCSM results for g.s. energies are taken for the maximum possible N_{max} at corresponding optimal frequencies. From the figure, it is seen that the g.s. energies of $^{18-20}\text{Ne}$ isotopes obtained from INOY interaction are close to the experimental results, while the other three interactions significantly underbind the g.s. of these nuclei. For $^{21-24}\text{Ne}$, the INOY interaction overbinds the corresponding g.s. compared to the experimental data. Overall, the INOY interaction is better for g.s. energy calculations due to its phenomenological non-local character at small distances. More binding energy due to non-local NN potential is explained in Ref. [62] for the case of triton binding energy.

Among the electromagnetic properties, the $E2$ transition strengths and moments of the Ne isotopes are not

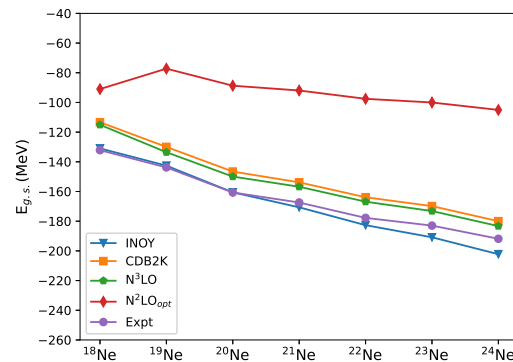


FIG. 5. A-dependence of the calculated g.s. energies using INOY, CDB2K, N^3LO and $\text{N}^2\text{LO}_{opt}$ NN interactions are compared to the experimental results.

TABLE II. Electromagnetic observables of $^{18-24}\text{Ne}$ corresponding to the largest N_{max} at their optimal HO frequencies. Quadrupole moments, magnetic moments, g.s. energies, $E2$ and $M1$ transitions are in barn (b), nuclear magneton (μ_N), MeV, $e^2 \text{ fm}^4$ and μ_N^2 respectively. Experimental values are taken from Refs. [72, 73].

^{18}Ne	EXPT	INOY	CDB2K	N^3LO	$\text{N}^2\text{LO}_{opt}$
$Q(2^+)$	NA	-0.014	-0.087	-0.102	-0.001
$\mu(2^+)$	NA	3.393	2.527	2.339	3.397
$E_{g.s.}(0^+)$	-132.143	-130.955	-113.333	-115.057	-90.993
$B(E2; 2_1^+ \rightarrow 0_1^+)$	49.6(50)	7.097	19.727	25.143	7.490
$B(E2; 4_1^+ \rightarrow 2_1^+)$	24.9(34)	5.614	13.566	17.260	5.704
^{19}Ne	EXPT	INOY	CDB2K	N^3LO	$\text{N}^2\text{LO}_{opt}$
$Q(5/2_1^+)$	NA	-0.059	-0.078	-0.089	-0.061
$\mu(5/2_1^+)$	-0.740(8)	-0.556	-0.464	-0.492	-0.852
$E_{g.s.}(1/2^+)$	-143.780	-142.584	-129.948	-133.522	-77.224
$B(E2; 5/2_1^+ \rightarrow 1/2_1^+)$	39.7(15)	8.868	15.543	20.044	7.324
$B(M1; 3/2_1^+ \rightarrow 5/2_1^+)$	0.89(50)	2.826	2.867	2.848	2.599
^{20}Ne	EXPT	INOY	CDB2K	N^3LO	$\text{N}^2\text{LO}_{opt}$
$Q(2^+)$	-0.23	-0.065	-0.082	< 0.001	-0.730
$\mu(2^+)$	1.08	1.044	1.025	1.022	1.044
$E_{g.s.}(0^+)$	-160.645	-160.545	-146.558	-149.939	-88.717
$B(E2; 2_1^+ \rightarrow 0_1^+)$	65.4(32)	10.346	16.182	< 0.001	16.483
$B(E2; 4_1^+ \rightarrow 2_1^+)$	71.0(64)	12.567	19.964	< 0.001	11.706
^{21}Ne	EXPT	INOY	CDB2K	N^3LO	$\text{N}^2\text{LO}_{opt}$
$Q(3/2_1^+)$	0.1016(8)	0.045	0.055	0.060	0.044
$\mu(3/2_1^+)$	-0.66170(3)	-0.491	-0.792	-0.923	-1.221
$E_{g.s.}(3/2^+)$	-167.406	-170.655	-153.819	-156.790	-91.951
$B(E2; 9/2_1^+ \rightarrow 5/2_1^+)$	54.0(75)	8.545	14.336	19.720	8.737
$B(M1; 5/2_1^+ \rightarrow 3/2_1^+)$	0.1275(25)	0.202	0.151	0.167	0.087
^{22}Ne	EXPT	INOY	CDB2K	N^3LO	$\text{N}^2\text{LO}_{opt}$
$Q(2^+)$	-0.215	-0.060	-0.075	-0.086	-0.067
$\mu(2^+)$	0.65(2)	0.574	0.358	0.395	0.484
$E_{g.s.}(0^+)$	-177.770	-182.675	-163.860	-166.865	-97.551
$B(E2; 2_1^+ \rightarrow 0_1^+)$	46.72(66)	8.813	13.650	17.668	11.112
$B(E2; 4_1^+ \rightarrow 2_1^+)$	64.1(14)	11.856	18.001	21.011	16.417
^{23}Ne	EXPT	INOY	CDB2K	N^3LO	$\text{N}^2\text{LO}_{opt}$
$Q(5/2^+)$	0.145(13)	0.070	-0.045	-0.066	0.063
$\mu(5/2^+)$	-1.0794(10)	-0.798	-0.641	-0.766	-0.869
$E_{g.s.}(5/2^+)$	-182.971	-190.836	-169.836	-173.163	-100.0248
$B(M1; 3/2_1^+ \rightarrow 5/2_1^+)$	NA	0.007	0.034	0.098	0.658
^{24}Ne	EXPT	INOY	CDB2K	N^3LO	$\text{N}^2\text{LO}_{opt}$
$Q(2^+)$	NA	-0.011	-0.030	-0.068	-0.012
$\mu(2^+)$	NA	1.493	0.514	0.732	2.279
$E_{g.s.}(0^+)$	-191.840	-202.234	-179.995	-183.290	-105.037
$B(E2; 2_1^+ \rightarrow 0_1^+)$	28.0(66)	6.204	10.282	16.155	8.049
$B(E2; 4_1^+ \rightarrow 2_1^+)$	NA	7.254	9.883	13.406	6.623

in good agreement with the experimental data as shown in the Table II. Also, the quadrupole moments of neon isotopes mentioned in Table II are not in good agreement with the experimental data. We have noted that the rate of convergence of $E2$ observables is slow compared to the convergence of excitation energies. The $E2$ operators contain r^2 dependence term, making those observables sensitive to the long-range part of the nuclear wave functions. In order to get correct asymptotic behaviour of nuclear wave functions and converged results

for $E2$ observables, large N_{max} basis spaces are needed. The N^3LO interaction results are better for $E2$ observables than the other three interactions. Still, for N^3LO , we only get about half the experimental $E2$ transition strengths, and moments for neon isotopes expect ^{20}Ne . Similar kind of observations for $E2$ transition strengths was also reported in ref. [74] for ^{12}C and ^6Li using the importance truncated no-core shell model (IT NCSM). Unlike the case of $E2$ observables, the $M1$ observables do not depend on the spatial distance and show different

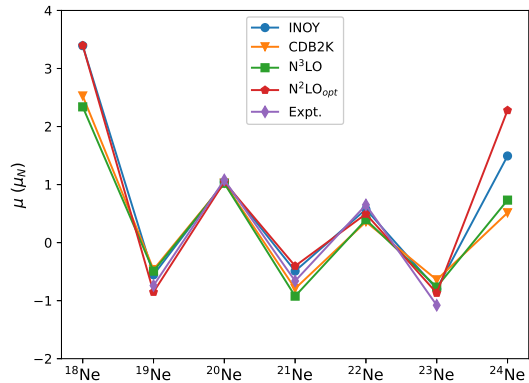


FIG. 6. Comparison between calculated magnetic moments at highest N_{max} using INOY, CDB2K, N^3LO and N^2LO_{opt} NN interactions with the experimental results.

convergence behaviour. The $M1$ observables are dependent only on the spin and angular momentum of nuclear states. Fig. 6 shows the magnetic moments of the studied neon isotopes. All four interactions well reproduce the general trend of experimental magnetic moments.

VI. POINT-PROTON RADII

In Table III, we have presented the numerical values of point-proton radii (r_p) obtained from INOY, CDB2K, and N^3LO interactions along with the experimental values for $^{18-24}Ne$ isotopes. These NCSM results for r_p are reported corresponding to highest possible N_{max} basis at their respective optimal frequencies. The root mean square point-proton distribution (r_p) is a long-range operator like the $E2$ transition operator, which is sensitive to the long-range part of nuclear wavefunctions. The experimental values of charge-radii are taken from the AD-NDT2013 compilation Ref. [75]. To calculate the point-proton radius from the experimental charge radius, the following formula is used:

$$\langle r^2 \rangle_p = \langle r^2 \rangle_c - \langle R_p^2 \rangle - \frac{N}{Z} \langle R_n^2 \rangle - \frac{3}{4m_p^2} \quad (4)$$

where, $\langle R_p^2 \rangle$ and $\langle R_n^2 \rangle$ are the squared charge radius of proton and neutron, respectively and the last term is the Darwin-Foldy term related to the relativistic correction in natural units. These values are taken to be $\langle R_p^2 \rangle^{1/2} = 0.8783(86)$ fm, $\langle R_n^2 \rangle = -0.1149(27)$ fm² [75] and $3/(4m_p^2) = 0.033$ fm² [76]. The squared point-proton radius relative to the center of mass of all nucleons is evaluated with

$$r_p^2 = \frac{1}{Z} \sum_{i=1}^Z |\vec{r}_i - \vec{R}_{CM}|^2. \quad (5)$$

The operator in the above equation is a two-body operator. It is reduced to a more suitable form involving one-body and two-body operators to evaluate two-body matrix elements for this operator. After finding the two-body matrix elements, the expectation value of the r_p operator is similar to the calculations of the ground-state energies.

TABLE III. The point-proton radii (r_p) calculated with INOY, CDB2K and N^3LO . These are given in fm.

r_p	Expt.	INOY	CDB2K	N^3LO
^{18}Ne	2.8490(84)	2.207	2.530	2.688
^{19}Ne	2.8893(49)	2.187	2.398	2.534
^{20}Ne	2.8885(34)	2.185	2.393	2.529
^{21}Ne	2.8530(43)	2.176	2.388	2.526
^{22}Ne	2.8374(49)	2.172	2.387	2.526
^{23}Ne	2.7956(79)	2.165	2.383	2.522
^{24}Ne	2.7876(86)	2.159	2.380	2.527

The r_p dependence on N_{max} and $\hbar\Omega$ for ^{18}Ne isotope corresponding to INOY, CDB2K and N^3LO interactions are shown in Fig. 7. From the figure, it can be seen that the curves of r_p as a function of $\hbar\Omega$ for different N_{max} appear to intersect at a common point for all the three interactions. For large N_{max} calculations, the $\hbar\Omega$ corresponding to this crossing point should be smaller than the variational minimum of the g.s. energy [77]. It is observed that at a lower HO frequency, the calculated r_p decrease with increasing N_{max} , while at a high HO frequency, it increases with increasing N_{max} . A region of calculated point-proton radii around the crossing point is independent of N_{max} . That crossover can be taken as a true converged point-proton radius [77, 78]. In this work, the intersection point of two r_p curves corresponding to two successive highest N_{max} are taken as the converged point-proton radius. In the first panel of Fig. 7, the r_p curves corresponding to $N_{max}=4$ and $N_{max}=6$ for INOY interaction cross each other approximately at 2.34 fm and this value is considered to be the point-proton radius obtained from INOY interaction. Similarly, the point-proton radii of ^{18}Ne obtained from CDB2K, and N^3LO are 2.51 fm and 2.60 fm, respectively. The point-proton radii for other neon isotopes are found similarly by calculating the intersection points of $N_{max}=2$ and $N_{max}=4$ curves corresponding to different NN interactions. The converged point-proton radii of $^{18-24}Ne$ isotopes obtained from INOY, CDB2K and N^3LO interactions are shown in Fig. 8 along with the experimental r_p extracted from Ref. [75]. From this figure, it can be seen that all the three interactions show the general trend of monotonic decrease of experimental point-proton radii from $^{19-24}Ne$. However, the calculated converged r_p is less than the experimental data. Among the three NN interactions, the CDB2K and N^3LO give better r_p values than those obtained from the INOY interaction. This observation can be correlated to the calculated g.s. energies shown in Fig. 5, that is, more binding of g.s. correspond

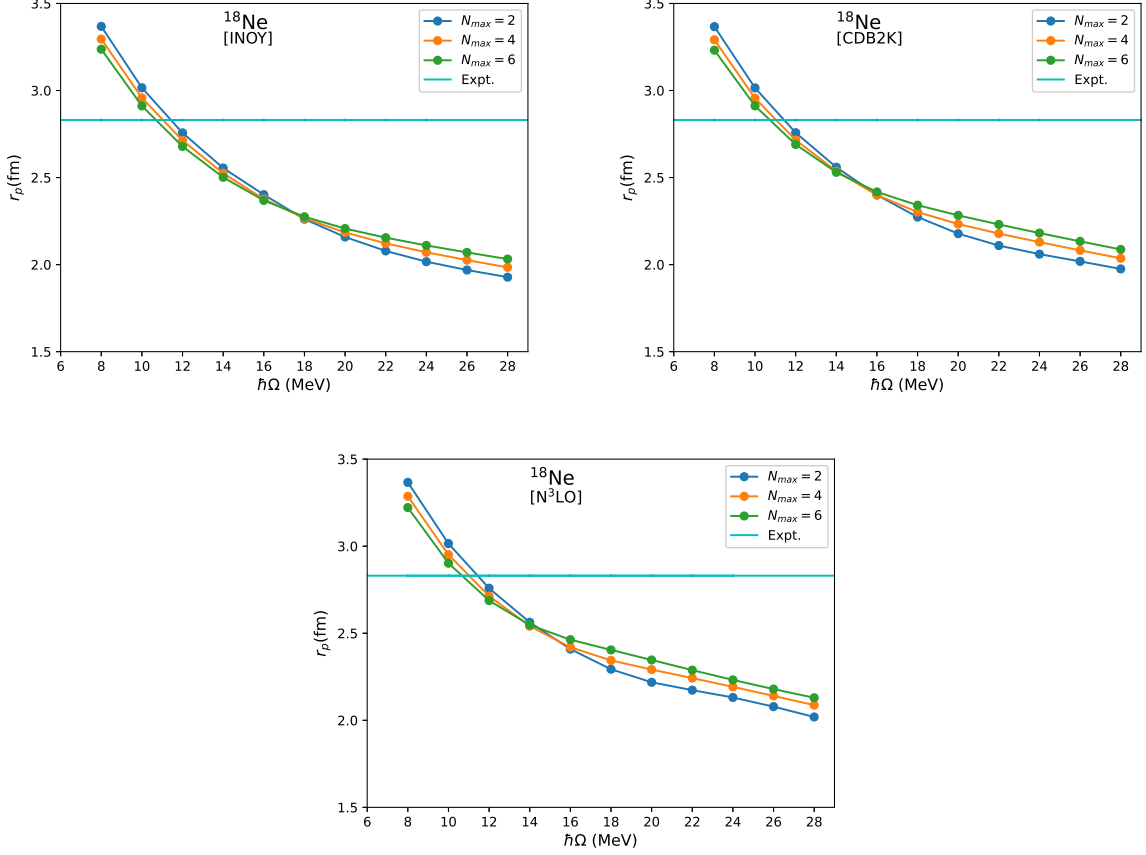


FIG. 7. Point-proton rms radius of ^{18}Ne g.s. as a function of $\hbar\Omega$.

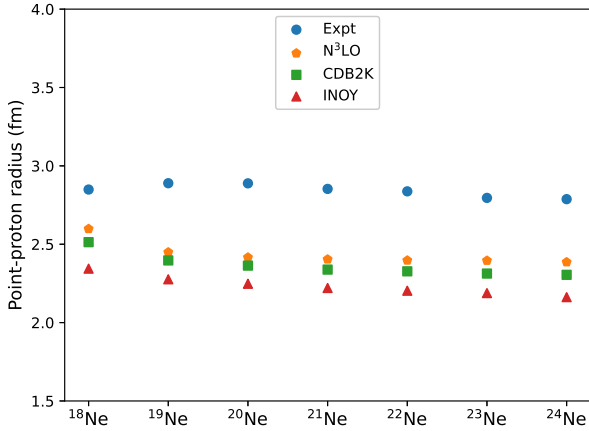


FIG. 8. Comparison of the NCSM results of point-proton rms radius with the INOY, CDB2K and $N^3\text{LO}$ NN interactions to the experimental data.

to a smaller radius.

For the case of ^{18}Ne , optimal $\hbar\Omega$ obtained for g.s. en-

ergy using INOY interaction is 20 MeV, whereas it is obtained to be $\hbar\Omega \approx 16$ MeV for g.s. point-proton radius. For CDB2K and $N^3\text{LO}$ interactions, the optimal $\hbar\Omega$ of ^{18}Ne g.s. energy and g.s. point-proton radii are almost same up to $N_{max} = 6$ calculations. The converged r_p of ^{18}Ne obtained from $N^3\text{LO}$ (up to $N_{max} = 6$) is almost 9 % less than the experimental r_p value. For other neon isotopes, this difference in r_p between the experimental and the calculated results from the same interaction is around 15 %, corresponding to NCSM calculations up to $N_{max} = 4$ basis space. So, we expect that for higher N_{max} calculations, the converged r_p will be close to the experimental data. Also, the $\hbar\Omega$ corresponding to the converged r_p will be small compared to the minimum of the variational ground-state energy.

From Fig. 8, a dip in the experimental as well as in the calculated r_p can be seen at $N = 14$ suggesting a shell closure at that point. Also, the decrease in r_p from ^{19}Ne to ^{24}Ne is an indication of a transition from deformation towards sphericity at the $N = 14$ shell closure [48].

VII. CONCLUSIONS

In this work, we have investigated spectroscopic properties of neon isotopes within *ab initio* no-core shell model using realistic NN interactions *i. e.* INOY, CDB2K, N^3LO and N^2LO_{opt} . We have studied low-energy spectra, electromagnetic properties, and point-proton radii with aforementioned interactions. We observed that the binding energy of $^{18-20}Ne$ obtained from INOY interaction is very close to the experimental g.s. binding energies, and for $^{21-24}Ne$ isotopes, it overbinds the corresponding g.s. The low-energy spectra obtained from all the four NN interactions provide good agreement with the experimental data.

Among the electromagnetic properties, the fast convergence of $M1$ observables is observed due to their independence on spatial coordinates. The $B(M1; 5/2_1^+ \rightarrow 3/2_1^+)$ of ^{21}Ne obtained from all the four interactions are close to the experimental $M1$ transition strength. Also, all these interactions reproduce the correct trend of experimental magnetic moments. On the other hand, the convergence of $E2$ observables is challenging to achieve in small model space calculations due to their r^2 -dependence. These observables are sensitive to the long-range behavior of nuclear wavefunctions, and a vast N_{max} basis space is needed to obtain converged results. The N^3LO provides better results for $E2$ transition strengths among the four realistic interactions. However, those values are only half of the experimental transition strengths.

The point-proton radius (r_p) is also sensitive to the long-range part of nuclear wavefunctions like the $E2$ observables, and to obtain the converged results for r_p , we used the ‘‘crossing point’’ method. We find out that the

point-proton radii calculated using N^3LO and CDB2K interactions for the g.s. of neon isotopes are better than INOY interaction, which is attributed to the fact that both N^3LO and CDB2K underbind the g.s. For N^3LO interaction, almost 6 % higher converged r_p is obtained for $N_{max} = 6$ compared to $N_{max} = 4$ calculations. So, better results for r_p can be expected for higher N_{max} calculations. We have noticed that the converged r_p decrease slowly from ^{19}Ne to ^{24}Ne making a dip at ^{24}Ne . It reflects a transition from deformation towards spherical shape at the $N = 14$ shell closure. This observation can also be seen from the decrease in the $B(E2; 2_1^+ \rightarrow 0_1^+)$ for even-Ne isotopes from ^{20}Ne to ^{24}Ne in Table II. We also observe the difference in optimal frequencies for the g.s. energy and the point-proton radius of these neon isotopes.

As diagonalization of large-matrix becomes a significant computational challenge for *ab initio* NCSM, recent modifications of conventional NCSM like IT-NCSM [74, 79] and SA-NCSM [36, 37] may help to study the full neon chain up to neutron drip line nuclei in the future. Also, the challenges of obtaining converged results for long-ranged observables can be tackled by the indirect approaches mentioned in Refs. [74, 80–82].

ACKNOWLEDGMENTS

We acknowledge financial support from SERB (India), CRG/2019/000556. We would like to thank Prof. Petr Navrátil for providing us his NN effective interaction code. We would also like to thank Prof. Christian Forssén for making available the pAntoine.

-
- [1] B. R. Barrett, P. Navrátil, and J. P. Vary, *Ab initio* no core shell model, **Prog. Part. Nucl. Phys.** **69**, 131 (2013).
 - [2] P. Maris, E. Epelbaum, R. J. Furnstahl, J. Golak, K. Hebeler, T. H  tther, H. Kamada, H. Krebs, Ulf-G. Meißner, J. A. Melendez *et al.*, Light nuclei with semilocal momentum-space regularized chiral interactions up to third order, **Phys. Rev. C** **103**, 054001 (2021).
 - [3] S. R. Stroberg, H. Hergert, S. K. Bogner, and J. D. Holt, Nonempirical interactions for the nuclear shell model: An update, **Annu. Rev. Nucl. Part. Sci.** **69**, 307 (2019).
 - [4] G. R. Jansen, M. D. Schuster, A. Signoracci, G. Hagen, and P. Navratil, Open *sd*-shell nuclei from first principles, **Phys. Rev. C** **94**, 011301(R) (2016).
 - [5] K. Hebeler, J. D. Holt, J. Men  ndez, and A. Schwenk, Nuclear Forces and Their Impact on Neutron-Rich Nuclei and Neutron-Rich Matter, **Annu. Rev. Nucl. Part. Sci.** **65**, 457 (2015).
 - [6] S. R. Stroberg, H. Hergert, S. K. Bogner, and J. D. Holt Nonempirical Interactions for the Nuclear Shell Model: An Update, **Annu. Rev. Nucl. Part. Sci.** **69**, 307 (2019).
 - [7] W. Leidemann and G. Orlandini, Modern *ab initio* approaches and applications in few-nucleon physics with $A \geq 4$, **Prog. Part. Nucl. Phys.** **68**, 158 (2013).
 - [8] R. Machleidt, K. Holinde, and C. Elster, The Bonn meson-exchange model for the nucleon-nucleon interaction, **Phys. Rep.** **149**, 1 (1987).
 - [9] R. Machleidt and D. R. Entem, Chiral effective field theory and nuclear forces, **Phys. Rep.** **503**, 1 (2011).
 - [10] E. Epelbaum, H.-W. Hammer, and U.-G. Meißner, Modern theory of nuclear forces, **Rev. Mod. Phys.** **81**, 1773 (2009).
 - [11] S. Weinberg, Phenomenological lagrangians, **Physica A** **96**, 327 (1979).
 - [12] S. Weinberg, Nuclear forces from chiral lagrangians, **Phys. Lett. B** **251**, 288 (1990).
 - [13] S. Weinberg, Effective chiral lagrangians for nucleon-pion interactions and nuclear forces, **Nucl. Phys. B** **363**, 3 (1991).
 - [14] P. Navrátil, S. Quaglioni, I. Stetcu, and B. R. Barrett, Recent developments in no-core shell-model calculations, **J. Phys. G: Nucl. Part. Phys.** **36**, 083101 (2009).
 - [15] B. A. Brown, The nuclear shell model towards the drip lines, **Prog. Part. Nucl. Phys.** **47**, 517 (2001).
 - [16] S. Cohen and D. Kurath, Effective interactions for the $1p$ shell, **Nucl. Phys.** **73**, 1 (1965).

- [17] B. A. Brown and W. A. Richter, New “USD” Hamiltonians for the sd shell, *Phys. Rev. C* **74**, 034315 (2006).
- [18] M. Honma, T. Otsuka, B. A. Brown, and T. Mizusaki, Shell-model description of neutron-rich pf -shell nuclei with a new effective interaction GXPF1, *Eur. Phys. J. A* **25**, 499 (2005).
- [19] O. Sorlin and M.-G. Porquet, Nuclear magic numbers: New features far from stability, *Prog. Part. Nucl. Phys.* **61**, 602 (2008).
- [20] T. Otsuka, A. Gade, O. Sorlin, T. Suzuki, and Y. Utsuno, Evolution of shell structure in exotic nuclei, *Rev. Mod. Phys.* **92**, 015002 (2020).
- [21] D. C. Zheng, J. P. Vary, and B. R. Barrett, Large-space shell-model calculations for light nuclei, *Phys. Rev. C* **50**, 2841 (1994).
- [22] P. Navrátil and B. R. Barrett, No-core shell-model calculations with starting-energy-independent multivalued effective interactions, *Phys. Rev. C* **54**, 2986 (1996).
- [23] P. Navrátil and B. R. Barrett, Large-basis shell-model calculations for p -shell nuclei, *Phys. Rev. C* **57**, 3119 (1998).
- [24] P. Navrátil and B. R. Barrett, Four-nucleon shell-model calculations in a Faddeev-like approach, *Phys. Rev. C* **59**, 1906 (1999).
- [25] P. Navrátil, J. P. Vary, and B. R. Barrett, Properties of ^{12}C in the *ab initio* nuclear shell model, *Phys. Rev. Lett.* **84**, 5728 (2000).
- [26] P. Navrátil, G. P. Kamuntavičius, and B. R. Barrett, Few-nucleon systems in a translationally invariant harmonic oscillator basis, *Phys. Rev. C* **61**, 044001 (2000).
- [27] P. Navrátil, J. P. Vary, and B. R. Barrett, Large-basis *ab initio* no-core shell model and its application to ^{12}C , *Phys. Rev. C* **62**, 054311 (2000).
- [28] P. Maris, J. P. Vary, and A. M. Shirokov, *Ab initio* no-core full configuration calculations of light nuclei, *Phys. Rev. C* **79**, 014308 (2009).
- [29] Y. Z. Ma, F. R. Xu, N. Michel, S. Zhang, J. G. Li, B. S. Hu, L. Coraggio, N. Itaco, and A. Gargano, Continuum and three-nucleon force in Borromean system: The ^{17}Ne case, *Phys. Lett. B* **808**, 135673 (2020).
- [30] A. Arima, S. Cohen, R. D. Lawson, and M. H. MacFarlane, A shell-model study of the isotopes of O, F and Ne, *Nucl. Phys. A* **108**, 94 (1968).
- [31] Y. Akiyama, A. Arima, and T. Sebe, The structure of the sd shell nuclei: (IV). ^{20}Ne , ^{21}Ne , ^{22}Ne , ^{22}Na and ^{24}Mg , *Nucl. Phys. A* **138**, 273 (1969).
- [32] H. Sagawa, X. R. Zhou, X. Z. Zhang, and T. Suzuki, Deformations and electromagnetic moments in carbon and neon isotopes, *Phys. Rev. C* **70**, 054316 (2004).
- [33] T. Tomoda and A. Arima, Coexistence of shell structure and cluster structure in ^{20}Ne , *Nucl. Phys. A* **303**, 217 (1978).
- [34] Y. Kanada-En’yo and H. Horiuchi, Coexistence of cluster and shell-model aspects in nuclear systems, *Front. Phys.* **13**, 132108 (2018).
- [35] M. Frosini, T. Duguet, J.-P. Ebran, B. Bally, T. Mongelli, T. R. Rodríguez, R. Roth, and V. Somà, Multi-reference many-body perturbation theory for nuclei, *Eur. Phys. J. A* **58**, 63 (2022).
- [36] T. Dytrych, K. D. Launey, J. P. Draayer, D. J. Rowe, J. L. Wood, G. Rosensteel, C. Bahri, D. Langr, and R. B. Baker, Physics of Nuclei: Key Role of an Emergent Symmetry, *Phys. Rev. Lett.* **124**, 042501 (2020).
- [37] O. M. Molchanov, K. D. Launey, A. Mercenne, G. H. Sargsyan, T. Dytrych, and J. P. Draayer, Machine learning approach to pattern recognition in nuclear dynamics from the *ab initio* symmetry-adapted no-core shell model, *Phys. Rev. C* **105**, 034306 (2022).
- [38] T. Abe, P. Maris, T. Otsuka, N. Shimizu, Y. Utsuno, and J. P. Vary, Ground-state properties of light $4n$ self-conjugate nuclei in *ab initio* no-core Monte Carlo shell model calculations with nonlocal NN interactions, *Phys. Rev. C* **104**, 054315 (2021).
- [39] S. R. Stroberg, J. Henderson, G. Hackman, P. Ruotsalainen, G. Hagen, and J. D. Holt, Systematics of $E2$ strength in the sd shell with the valence-space in-medium similarity renormalization group, *Phys. Rev. C* **105**, 034333 (2022).
- [40] P. Marević, J.-P. Ebran, E. Khan, T. Nikšić, and D. Vretenar, Quadrupole and octupole collectivity and cluster structures in neon isotopes, *Phys. Rev. C* **97**, 024334 (2018).
- [41] M. Thoennessen, Current status and future potential of nuclide discoveries, *Rep. Prog. Phys.* **76**, 056301 (2013).
- [42] D. S. Ahn, N. Fukuda *et al.*, Location of the neutron dripline at fluorine and neon, *Phys. Rev. Lett.* **123**, 212501 (2019).
- [43] Á. Koszorús, X. F. Yang, W. G. Jiang *et al.*, Charge radii of exotic potassium isotopes challenge nuclear theory and the magic character of $N = 32$, *Nat. Phys.* **17**, 439 (2021).
- [44] I. Angeli *et al.*, N and Z dependence of nuclear charge radii, *J. Phys. G: Nucl. Part. Phys.* **36**, 085102 (2009).
- [45] W. Geithner, T. Neff *et al.*, Masses and Charge Radii of $^{17-22}\text{Ne}$ and the Two-Proton-Halo Candidate ^{17}Ne , *Phys. Rev. Lett.* **101**, 252502 (2008).
- [46] K. Marinova, W. Geithner, M. Kowalska, K. Blaum, S. Kappertz, M. Keim, S. Kloos, G. Kotrotsios, P. Lievens, R. Neugart, H. Simon, and S. Wilbert, Charge radii of neon isotopes across the sd neutron shell, *Phys. Rev. C* **84**, 034313 (2011).
- [47] S. J. Novario, G. Hagen, G. R. Jansen, and T. Papenbrock, Charge radii of exotic neon and magnesium isotopes, *Phys. Rev. C* **102**, 051303(R) (2020).
- [48] S. Bagchi, R. Kanungo, W. Horiuchi, G. Hagen, T. D. Morris, S. R. Stroberg, T. Suzuki, F. Ameil, J. Atkinson, Y. Ayyad *et al.*, Neutron skin and signature of the $N = 14$ shell gap found from measured proton radii of $^{17-22}\text{N}$, *Phys. Lett. B* **790**, 251 (2019).
- [49] P. Doleschall and I. Borbély, Properties of the nonlocal NN interactions required for the correct triton binding energy, *Phys. Rev. C* **62**, 054004 (2000).
- [50] R. Machleidt, High-precision, charge-dependent Bonn nucleon-nucleon potential, *Phys. Rev. C* **63**, 024001 (2001).
- [51] D. R. Entem and R. Machleidt, Accurate charge-dependent nucleon-nucleon potential at fourth order of chiral perturbation theory, *Phys. Rev. C* **68**, 041001(R) (2003).
- [52] A. Ekström, G. Baardsen, C. Forssén, G. Hagen, M. Hjorth-Jensen, G. R. Jansen, R. Machleidt, W. Nazarewicz, T. Papenbrock, J. Sarich *et al.*, Optimized chiral nucleon-nucleon interaction at next-to-next-to-leading order, *Phys. Rev. Lett.* **110**, 192502 (2013).
- [53] S. Ôkubo, Diagonalization of Hamiltonian and Tamm-Dancoff equation, *Prog. Theor. Phys.* **12**, 603 (1954).

- [54] K. Suzuki and S. Y. Lee, Convergent theory for effective interaction in nuclei, *Prog. Theor. Phys.* **64**, 2091 (1980).
- [55] K. Suzuki, Construction of Hermitian effective interaction in nuclei: General relation between Hermitian and non-Hermitian forms, *Prog. Theor. Phys.* **68**, 246 (1982).
- [56] K. Suzuki and R. Okamoto, Effective interaction theory and unitary-model-operator approach to nuclear saturation problem, *Prog. Theor. Phys.* **92**, 1045 (1994).
- [57] S. K. Bogner, R. J. Furnstahl, and R. J. Perry, Similarity renormalization group for nucleon-nucleon interactions, *Phys. Rev. C* **75**, 061001 (2007).
- [58] E. D. Jurgenson, P. Navrátil, and R. J. Furnstahl, Evolving nuclear many-body forces with the similarity renormalization group, *Phys. Rev. C* **83**, 034301 (2011).
- [59] D. H. Gloeckner and R. D. Lawson, Spurious center-of-mass motion, *Phys. Lett. B* **53**, 313 (1974).
- [60] P. Doleschall, I. Borbély, Z. Papp, and W. Plessas, Nonlocality in the nucleon-nucleon interaction and three-nucleon bound states, *Phys. Rev. C* **67**, 064005 (2003).
- [61] P. Doleschall, Influence of the short range nonlocal nucleon-nucleon interaction on the elastic $n - d$ scattering: Below 30 MeV, *Phys. Rev. C* **69**, 054001 (2004).
- [62] R. Machleidt, F. Sammarruca, and Y. Song, Nonlocal nature of the nuclear force and its impact on nuclear structure, *Phys. Rev. C* **53**, R1483(R) (1996).
- [63] R. Machleidt, The meson theory of nuclear forces and nuclear structure, *Adv. Nucl. Phys.* **19**, 189 (1989).
- [64] D. Logoteta, Optimized chiral N2LO interactions in nuclear matter, *Eur. Phys. J. A* **54**, 111 (2018).
- [65] R. B. Wiringa, V. G. J. Stoks, and R. Schiavilla, Accurate nucleon-nucleon potential with charge-independence breaking, *Phys. Rev. C* **51**, 38 (1995).
- [66] E. Caurier and F. Nowacki, Present status of shell model techniques, *Acta Phys. Pol. B* **30**, 705 (1999).
- [67] E. Caurier, G. Martínez-Pinedo, F. Nowacki, A. Poves, and A. P. Zuker, The shell model as a unified view of nuclear structure, *Rev. Mod. Phys.* **77**, 427 (2005).
- [68] C. Forssén, B. D. Carlsson, H. T. Johansson, D. Sääf, A. Bansal, G. Hagen, and T. Papenbrock, Large-scale exact diagonalizations reveal low-momentum scales of nuclei, *Phys. Rev. C* **97**, 034328 (2018).
- [69] A. Saxena and P. C. Srivastava, *Ab initio* no-core shell model study of neutron-rich nitrogen isotopes, *Prog. Theor. Exp. Phys.* **2019**, 073D02 (2019).
- [70] A. Saxena and P. C. Srivastava, *Ab initio* no-core shell model study of $^{18-23}\text{O}$ and $^{18-24}\text{F}$ isotopes, *J. Phys. G: Nucl. Part. Phys.* **47**, 055113 (2020).
- [71] P. Choudhary, P. C. Srivastava, and P. Navrátil, *Ab initio* no-core shell model study of $^{10-14}\text{B}$ isotopes with realistic NN interactions, *Phys. Rev. C* **102**, 044309 (2020).
- [72] Data extracted using the NNDC World Wide Web site from the ENSDF, <https://www.nndc.bnl.gov/ensdf/>.
- [73] IAEA, <https://www-nds.iaea.org/nuclearmoments/>.
- [74] A. Calci and R. Roth, Sensitivities and correlations of nuclear structure observables emerging from chiral interactions, *Phys. Rev. C* **94**, 014322 (2016).
- [75] I. Angeli *et al.*, Table of experimental nuclear g.s charge radii: An update, *At. Data Nucl. Data Tables*, **99**, 69 (2013).
- [76] A. Ekström, G. R. Jansen, K. A. Wendt, G. Hagen, T. Papenbrock, B. D. Carlsson, C. Forssén, M. Hjorth-Jensen, P. Navrátil, and W. Nazarewicz, Accurate nuclear radii and binding energies from a chiral interaction, *Phys. Rev. C* **91**, 051301(R) (2015).
- [77] A. M. Shirokov, I. J. Shin, Y. Kim, M. Sosonkina, P. Maris, and J. P. Vary, N3LO NN interaction adjusted to light nuclei in *ab exitu* approach, *Phys. Lett. B* **761**, 87 (2016).
- [78] M. A. Caprio, P. Maris, and J. P. Vary, Halo nuclei ^6He and ^8He with the Coulomb-Sturmian basis, *Phys. Rev. C* **90**, 034305 (2014).
- [79] R. Roth, Importance truncation for large-scale configuration interaction approaches, *Phys. Rev. C* **79**, 064324 (2009).
- [80] S. L. Henderson, T. Ahn, M. A. Caprio *et al.*, First measurement of the $B(E2; 3/2^- \rightarrow 1/2^-)$ transition strength in ^7Be : Testing *ab initio* predictions for $A = 7$ nuclei, *Phys. Rev. C* **99**, 064320 (2019).
- [81] M. A. Caprio and P. J. Fasano, *Ab initio* prediction of $E2$ strengths in ^8Li and its neighbors by normalization to the measured quadrupole moment, [arXiv:2206.05628v1](https://arxiv.org/abs/2206.05628v1) (2022).
- [82] M. A. Caprio and P. J. Fasano, Robust *ab initio* prediction of nuclear electric quadrupole observables by scaling to the charge radius, *Phys. Rev. C* **105**, L061302 (2022).